SCALES AND SPECTRA OF TURBULENCE OVER THE GULF STREAM DURING OFFSHORE CYCLOGENESIS

NEERAJA C. REDDY and SETHU RAMAN

Department of Marine, Earth and Atmospheric Sciences, North Carolina State University, Raleigh, NC 27695-8208, U.S.A.

(Received in final form 8 September, 1993)

Abstract. Turbulence structure of the marine boundary layer (MBL) over the Gulf Stream and the adjacent coastal waters during the development of a storm is discussed. Prestorm conditions prevailed on 9 February and a meso-low formed on 10 February which intensified into an offshore cyclone on 11 February. Observations from aircraft, buoys and ships were made as part of the Genesis of Atlantic Lows Experiment (GALE, 86) during these three days. Analysis of the high frequency (20 Hz) turbulence data collected from low-level flights by the NCAR King Air and Electra indicates the effect of the storm development on the turbulence structure of the MBL.

Observational data over the stable region near the coast on 10 February revealed the presence of internal gravity waves. Spectral analysis indicates that the size and energy of the eddies increased over the Gulf Stream and also increased as the storm developed. Results obtained using conditional sampling techniques suggest that intense narrower warm updrafts dominate the total heat flux. The broader, less intense cool downdrafts seem to occupy a large portion of the Gulf Stream.

1. Introduction

Recent observational studies have examined the dynamics of the atmospheric marine boundary layer (MBL) due to sea surface temperature (SST) discontinuities during the 1986 Frontal Air–Sea Interaction Experiment (FASINEX) and the 1986 Genesis of Atlantic Lows Experiment (GALE). Results from FASINEX, which are considered valid for open ocean temperature fronts, have contrasted the vertical structure of the MBL on the warm side of the oceanic front with that on the cold side (Herbster, 1990). In addition, several numerical studies have been conducted to investigate the effects of strong baroclinicity in the MBL (for example, Huang and Raman, 1988, 1990, 1991a, 1991b). A numerical study by Wai and Stage (1989) using a two-dimensional model investigated circulation in the MBL near the Gulf Stream. Holt and Raman (1992) provided evidence that the coastal frontal surface that is generated near the Gulf Stream during winter plays an important role in the three-dimensional atmospheric circulation. Huang and Raman (1990) found similar circulations in their numerical simulations with intensification of the flow by the accumulated heat fluxes at later stages.

This paper describes the turbulent structure in the MBL during three different synoptic conditions. Quasi-stationary conditions prevailed on 9 February, a meso-low formed on 10 February and intensified into an offshore depression on 11 February. For this paper, observations collected during GALE IOP #5 are used. GALE was conducted in the mid-Atlantic coastal region of the United States from

Boundary-Layer Meteorology **68**: 387–417, 1994.

15 January to 15 March, 1986 (Dirks *et al.*, 1988), the main objective being to investigate the development of east coast storms. In the present study, the Electra and the King Air aircraft measurements from 9–11 February, 1986 are used to compute the conditional sampling averages of relevant physical parameters during this period. Spectral analysis has been carried out to compare the scales of turbulent motion. Observations and results are compared to other boundary-layer experiments to help understand differences in boundary-layer processes and structure. King Air and Electra aircraft data from 9–11 February are the primary data sets.

2. Observations and Methodology

Observations during GALE have been discussed in detail by Mercer and Kreitzberg (1986), Dirks *et al.* (1988) and Raman and Riordan (1988). A variety of National Weather Service and GALE surface and upper-air data are used in this study. Observations made with the NCAR King Air and Electra research flights on 10 February 1986 will be examined to study the mesoscale circulation over the Gulf Stream and a Gulf Stream filament. Aircraft data are the primary dataset, but supporting observations from special surface data and the Cross-Chain Loran Atmospheric Sounding Systems (CLASS) will also be used. The upper air sounding data were obtained from CLASS rawinsondes, mini-radiosondes, special NWS rawinsondes and Omega dropwindsondes.

The special GALE surface data were obtained from 51 PAM II sites, eight instrumented GALE research buoys, NOAA buoys and platforms and one research vessel, R/V Cape Hatterras. The sea surface temperature (SST) field was derived from NOAA-9 infrared imagery. This 1.1 km high resolution imagery helped in resolving the strong sea surface temperature gradients associated with the Gulf Stream and its filaments. Reports by observers onboard the King Air were useful in providing observations not easily obtainable from synoptic weather maps, ship or dropwindsonde data. These observations mostly pertained to the type, height and structure of the clouds.

The flight track for 9–11 February is shown in Figure 1. Position of the western edge of the Gulf Stream (heavy solid line) on 10 February is indicated. This was obtained from the AVHRR (Advanced Very High Resolution Radiometer) data. The heavy dashed line indicates the eastern edge of the Gulf Stream. Positions A and B indicate regions of vertical profiling on 9 February (Figure 2a). A level-wing descent from 1500 m was first flown at A (35.9 N, 75 W) at approximately 1630 UTC over the cold shelf waters (SST = 12–14 °C). The flight proceeded at 40 m altitude from A to C (35.6 N, 73.8 W), located east of the Gulf Stream core (SST = 20 °C) for a distance of 120 km. The flight then made a return transect from C to B (35.8 N, 74.25 W), located over the Gulf Stream (SST = 24 °C) at 40 m altitude. At B a vertical stack consisting of a series of level 240 to 360 s legs (19.2 to 28.8 km in length at an aircraft speed of 80 m s^{-1}) were flown at five

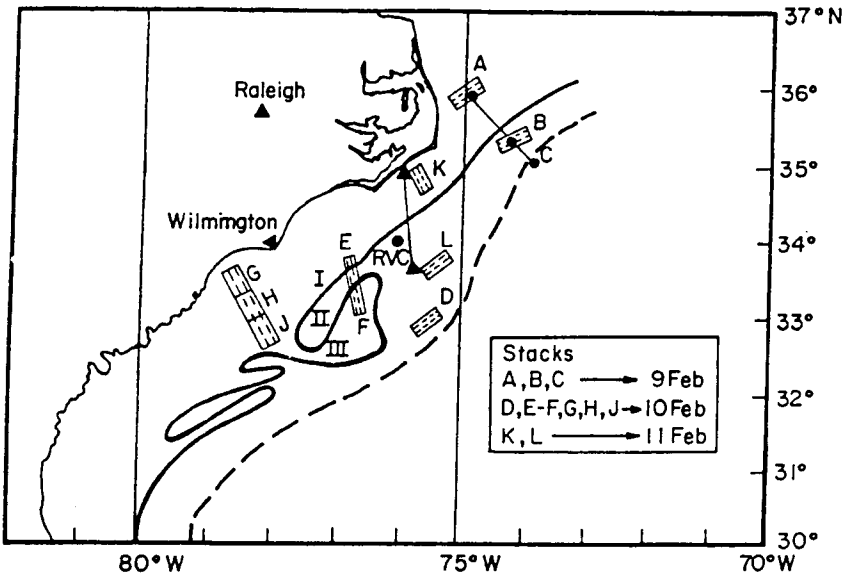

Fig. 1. Flight tracks of King Air and Electra aircraft from 9–11 February. Stacks A, B and C were taken on 9 February, stacks D, E–F, G, H and J were taken on 10 February in the region of meso-low development and K and L were taken on 11 February in the region of offshore cyclogenesis. RVC indicates the location of Research Vessel/Cape Hatteras.

altitudes. One level-flight was also made above cloud top in the free atmosphere. The flight from B to A was approximately at 400 m altitude (roughly 45 km between A and B). A vertical stack was flown at A (1830 UTC) similar to that at B. Upon completion of the last leg at A (altitude of 2000 m), a level-wing descent was flown at 1850 UTC.

On 10 February, the King Air flight took a level-wing descent from 1500 m at D (32.8 N, 75.8 W) over the Gulf Stream waters (SST = 24 °C) at 1300 UTC (Figure 2b). A vertical stack consisting of a series of level 300–400 s legs (23.1–30.8 km in length at an aircraft speed of 77 m s^{-1}) at four altitudes in the subcloud layer was flown. The flight departed from Wilmington at 1600 UTC. A vertical stack consisting of a series of level 300–720 s (23.1–55.5 km in distance at an aircraft speed of 77 m s^{-1}) at four altitudes in the subcloud layer was flown at E–F (33 N, 77 W). This stack was flown perpendicular to a Gulf Stream "filament", a tongue-like extrusion of the Gulf Stream warm waters into cold mid shelf waters (see Figure 1).

The NCAR Electra aircraft at about 1800 UTC flew seven vertical cross-sections at altitudes of 50, 90, 150, 200, 320, 630 and 1200 m (SST = 9–23 °C and location = 33 N, 77 W) for 12 to 20 min (100–140 km) at an aircraft speed of 110 m s^{-1}. The length of each leg flown by Electra aircraft is divided into three to four segments (approximate duration of 4–5 min). The first segment represents near shore waters

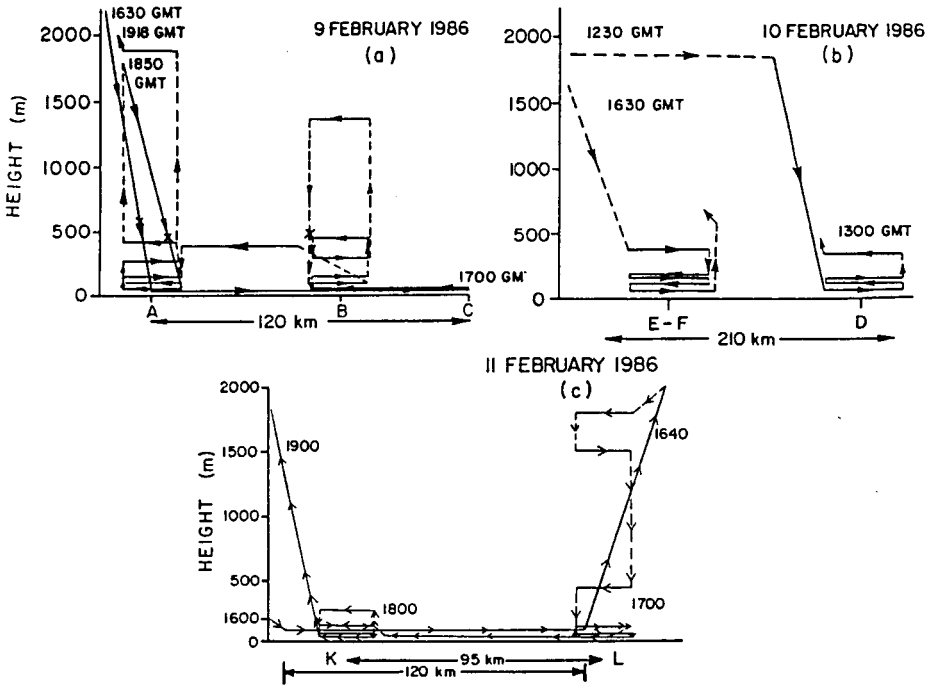

Fig. 2. Vertical cross-sections of the flight track on (a) 9 February, (b) 10 February and (c) 11 February, 1986.

(G) with SST between 10 and 13 °C, the second represents near shore shelf waters (H) with SST between 13 and 16 °C, the third represents mid-shelf waters (H–J) with SST between 16 and 19 °C and the fourth represents Gulf Stream waters (J) with SST between 19 and 22 °C. Scientists on board the Electra reported multiple cloud layers.

The initial flight plans of King Air aircraft on 11 February were to obtain flux profiles over the mid shelf front and the Gulf Stream core during a period of southwesterly flow and to investigate coastal frontal structure. The flight track on 11 February is shown in Figure 1. The King Air aircraft departed Raleigh at 1300 UTC and flew offshore towards the Gulf Sheam for about 110–120 km. A six-level stack (33.5 N, 75.6 W) was flown at 1700 UTC over the core of the Gulf Stream (L) at 30, 90, 150, 400, 1500 and 1750 m altitudes (Figure 2c). A vertical descent profile (SST = 24.2 °C) was then performed at this same location. After completing the stack at L, the King Air flew north towards the mid shelf waters at 30 m altitude for about 90–100 km and flew a four-level stack (34.5 N, 76.5 W) over the mid shelf front (position K) at 40, 90, 150 and 250 m altitudes at 1800 UTC. After this stack, King Air flew one vertical ascent profile (SST = 13 °C) over the cold waters at 1900 UTC.

Orientation of the vertical stacks in the MBL was aligned perpendicular to the mean wind directions for optimal determination of turbulent fluxes (LeMone, 1973); and roughly parallel to SST isotherms to avoid conditions of large horizontal inhomogeneity in the time series data. Stacks B, D and L on 9, 10 and 11 February, respectively satisfied these conditions.

Instrumentation on the King Air aircraft is similar to that on the Electra aircraft. A description of the instrumentation on board the Electra is discussed in detail by LeMone and Pennell (1980) and Lenschow and Spyers-Duran (1986). Only a brief discussion of the primary aircraft mean and turbulent data and analysis employed in this study is included here. Both low-rate (1 Hz) and high-rate (20 Hz) data were obtained from the aircraft instrumentation system.

On board the aircraft, ambient temperature was measured by a Rosemount temperature probe, dew point by an EG&G dewpoint hygrometer and pressure by a Rosemount pressure transducer. A radome gust probe with pressure ports on the nose of the King Air was used for sensing air motion. Both mean horizontal wind and turbulent fluctuations of the three air velocity components were obtained from the radome and the inertial navigation system (INS). The wind components were obtained by subtraction of the airplane velocity, measured by the INS, from the velocity of the air, obtained from the differential pressure measured across the ports on the radome (Brown *et al.*, 1983).

Calibration of the 20 Hz Lyman-α humidity data used the method of Lind and Shaw (1990) in which a linear regression of Lyman-α data on 1 Hz hygrometer data was performed. Values of SST were determined from the downward-viewing radiometer (not corrected for reflected sky radiation or atmospheric absorption).

Mean and turbulence values over the length of each flight leg were then detrended by linear regression. Any spurious spikes, represented by values exceeding three standard deviations were also removed. Means, standard deviations and fluxes were then computed from detrended data for each leg. Turbulent fluxes were calculated using simple statistics involving the covariance and correlation between two variables of interest. Spectral analysis was performed using the fast fourier transform (FFT) technique to obtain dominant scales of motion.

3. Synoptic and Mesoscale Conditions

A high pressure system dominated the east coast of the United States at 18 UTC on 9 February, causing northerly offshore winds (Figure 3a). In the GALE region (offshore of Carolinas, 30–37 N, 70–80 W), gradual veering of the offshore winds from north–northeasterly to east–northeasterly accompanied the eastward shift of the anticyclone. Over land (east coast of the U.S), however, the wind direction remained northeasterly as a ridge of high pressure extended southwestward along the coast, east of the Appalachians. At 06 UTC (Figure 3b) on 10 February, a trough extended southwest from offshore of North Carolina towards the South

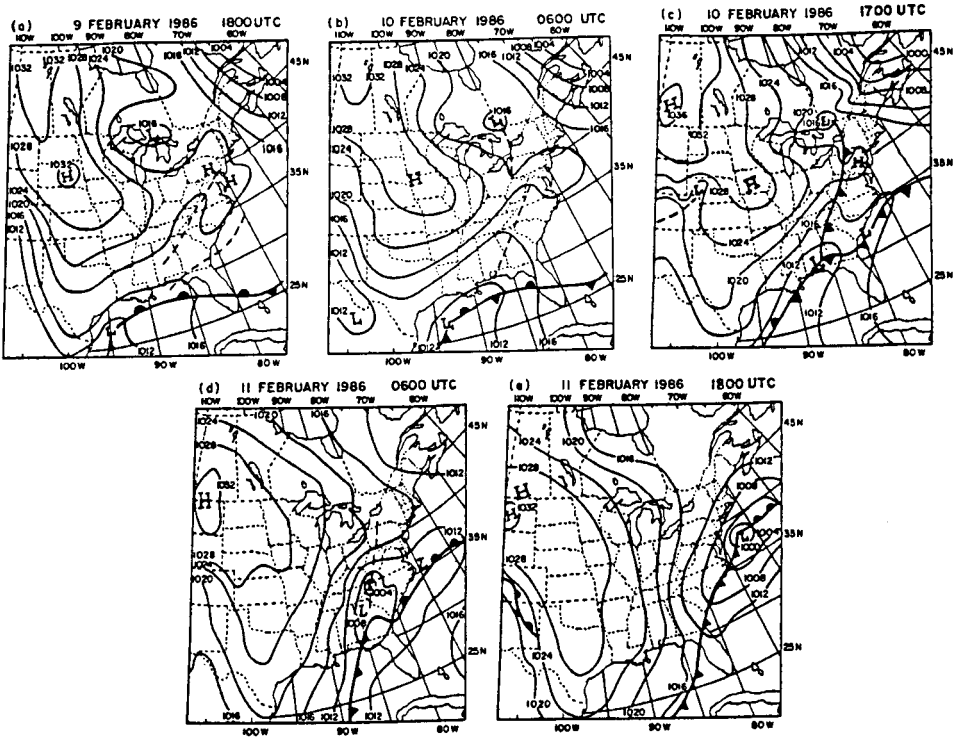

Fig. 3. NMC surface pressure analysis for (a) 18 UTC on 9 February, (b) 06 UTC on 10 February, (c) 18 UTC on 10 February, (d) 06 UTC on 11 February, and (e) 18 UTC on 11 February, 1986. Isobars are given every 4 mb.

Carolina coast and a low pressure system developed off North Carolina. From 15 UTC-21 UTC (Figure 3c) on 10 February, a stationary front was off the coast almost parallel to the Gulf Stream. Aircraft observations taken during this period indicated a mesoscale circulation which may have led to a meso-low over the Gulf Stream region (Figure 4). At 06 UTC (Figure 3d) on 11 February, a mid- tropospheric trough was located over Alabama. This trough migrated offshore by 12 UTC on 11 February (not shown) and might have caused the intensification of the meso-low.

Mesoscale surface analysis offshore on 9 February (not shown) indicated weak (1–2 $m\,s^{-1}$) northerly winds along the coast. Over the Gulf Stream, however, winds were northeasterly and strong (10 $m\,s^{-1}$). The mesoscale analysis at 1700 UTC 10 February is shown in Figure 4. The streamline analysis (Figure 4a) indicates two confluence zones (heavy solid lines) and a diffluence zone in between. The winds increased by a factor of two from 4.8 $m\,s^{-1}$ over mid shelf waters to 9.5 $m\,s^{-1}$ at the western edge of the Gulf Stream. This circulation developed into

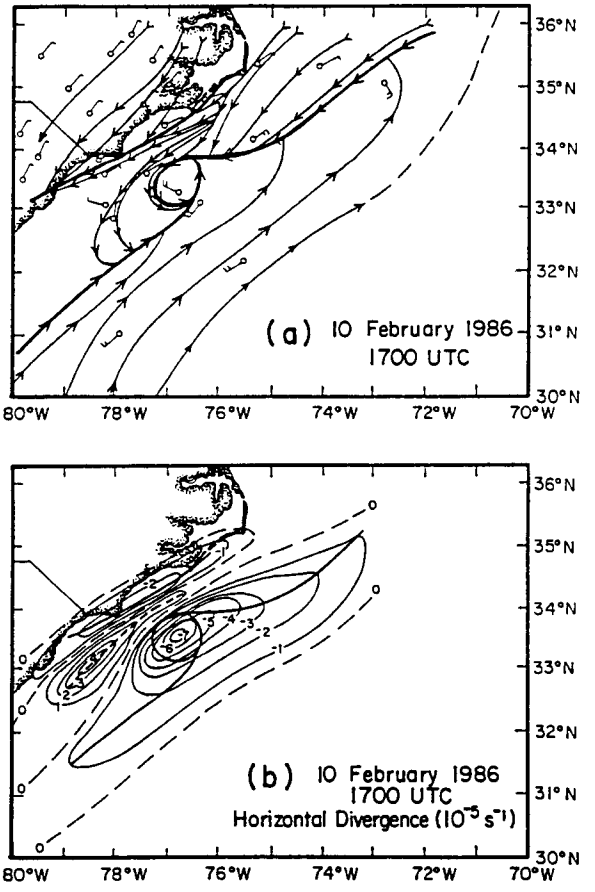

Fig. 4. Mesoscale analysis on 10 February at 17 UTC. (a) Streamline analysis. Heavy solid lines indicate the confluence zones. (b) Contours of estimated convergence. Heavy solid lines indicate the convergence zones and heavy dashed lines indicate the divergence zone.

a meso-low on 10 February by 17 UTC (Figure 4a). The contours of computed horizontal divergence are shown in Figure 4b. This analysis indicates two low-level mesoscale convergence zones, one near the western edge of the Gulf Stream ($7.8 \times 10^{-5}\,s^{-1}$, heavy solid line) and the other near the coastal waters offshore of Wilmington ($3.4 \times 10^{-5}\,s^{-1}$, heavy solid line) with a divergence zone in between ($3.1 \times 10^{-5}\,s^{-1}$, heavy dashed line). Similar convergence/divergence zones were also observed by Riordan (1990) and Holt and Raman (1990) for other days during coastal frontogenesis. Mesoscale analysis on 11 February indicated a northwesterly flow near the coast and southwesterly flow over the western Atlantic. The wind speeds increased offshore due to the deepening of the surface cyclone offshore of the Carolinas as a mid-tropospheric trough moved into the region.

TABLE I

Boundary-layer fluxes and parameters from 9–11 February. CS and GS indicate cold coastal shelf waters and Gulf Stream waters, respectively. Observations at A and B were on 9 February, at D were on 10 February and at L were on 11 February. Stacks B, D and L are over the Gulf Stream. Units are in MKS, unless specified

Region	A CS	B GS	D GS	L GS
Time (UTC)	1830	1700	1300	1700
SST (C)	10.0	24.0	24.0	24.3
h	300	600	700	1600
w_*	0.63	1.45	1.15	2.4
u_*	0.20	0.45	0.37	0.74
θ_*	0.04	0.10	0.05	0.03
q_*	0.01	0.02	0.05	0.03
$\overline{(w\theta_v)}_s$	0.024	0.15	0.06	0.07
$\overline{(w'q')}_s$	0.006	0.028	0.056	0.067
$\overline{(u'w')}_s$	−0.03	0.09	−0.02	−0.42
$\overline{(v'w')}_s$	0.02	0.18	−0.11	−0.32
$-L$	24	45	63	435
$-h/L$	12	18	12	3.5
H ($W m^{-2}$)	30	185	75	85
E ($W m^{-2}$)	28	85	170	200

4. Discussion of Results

In analyzing the turbulent structure of the MBL, the high-rate (20 Hz) data were utilized to generate statistical parameters representative of the atmospheric turbulent properties. Appropriate scaling parameters, viz., the surface friction velocity (u_*), the convective velocity scale (w_*), the convective temperature scale (θ_*), the convective humidity scale (q_*), convective time scale (t_*) and the Monin–Obukhov length (L), were calculated. Aircraft flux data collected at the lowest flight levels were linearly extrapolated to the surface to get the surface fluxes.

Table 1 summarizes the above values at various heights and locations sampled by the King Air and Electra aircraft. Also given are surface sensible (H) and latent (E) heat fluxes:

$$H = \rho c_p (\overline{w'\theta'})_0 , \tag{1}$$

$$E = \rho L_v (\overline{w'q'})_0 , \tag{2}$$

where ρ is density, c_p is specific heat of air (1004 J kg^{-1} K^{-1}) and L_v is the latent heat of vaporization (2.45×10^6 J kg^{-1}).

On 9 February, a SST difference of 14C was observed between the coastal waters and the Gulf Stream (Table I). The boundary-layer height doubled over the Gulf Stream. Surface fluxes of total heat increased by a factor of five and surface friction velocity increased by a factor of 2.2 over the Gulf Stream compared

to values over the cold shelf waters. Convective velocity scale (w_*) increased by almost a factor of five due to the increase in the sensible and latent heat fluxes and strong convection over the Gulf Stream. The boundary layer was convective over both locations A and B as indicated by the Monin–Obhukov length (Table I).

On 10 February, the SST difference from J (mid shelf waters, MS) to D (Gulf Stream) was only about 4 °C (not shown in Table I). However, the boundary-layer height increased by about 75% and the total heat flux increased by a factor of about seven over the Gulf Stream. Smaller heat fluxes over location J is because of its proximity to the divergence zone. Winds were very light in this region ($3\ m\ s^{-1}$). Friction velocity increased by about 50% but the convective velocity increased by a factor of two over the Gulf Stream.

A comparison of boundary-layer fluxes and parameters from prestorm conditions (9 February) to meso-low development (10 February) to offshore cyclogenesis (11 February) over the Gulf Stream indicates a significant increase in boundary-layer height as the storm developed on 11 February. This increase is accompanied by an increase in total heat flux. But for the other two days, February 9 and 10, there is no significant difference in values of the mean turbulence parameters.

4.1. Spatial variation of surface turbulent heat fluxes

The total heat flux (sensible + latent) increased from cold shelf waters to the Gulf Stream on all three days. Figures 5a, 5b and 5c show the spatial variation of heat fluxes on 9, 10 and 11 February, respectively. Values at A, B and C in Figure 5a are aircraft observations and the rest of the data were obtained from ship and buoy stations offshore. The total heat flux was about $150\ W\ m^{-2}$ over the Gulf Stream. However, the aircraft data at the Gulf Stream edge (indicated by * in Figure 5a) show an heat flux of $340\ W\ m^{-2}$. As the cooler air from the upwelling region crossed the Gulf Stream, a large increase in wind speed and vertical temperature gradient caused a large heat flux. The heat fluxes again decreased towards the Sargaso sea region east of the Gulf Stream to as low as $50\ W\ m^{-2}$.

The spatial variation of fluxes on 10 February is shown in Figure 5b (negative heat fluxes indicate stable conditions). The heat fluxes are on the order of $250\ W\ m^{-2}$ and above over the Gulf Stream in the region of the meso-low. The latent heat flux gradient weakened considerably (Table I) westward over the cold shelf waters where divergent flow was present.

Figure 5c shows the spatial variation of fluxes on 11 February during offshore cyclogenesis. The total heat fluxes increased considerably over the Gulf Stream compared to previous days, reaching an order of about $350\ W\ m^{-2}$. A comparison of heat fluxes at Research Vessel/Cape Hatteras (RVC, see Figure 1 for location) on all three days indicates that the values increased from $187\ W\ m^{-2}$ on 9 February to a value of $460\ W\ m^{-2}$ on 10 February during the formation of a meso-low and to about $530\ W\ m^{-2}$ on 11 February during the intensification of the cyclone.

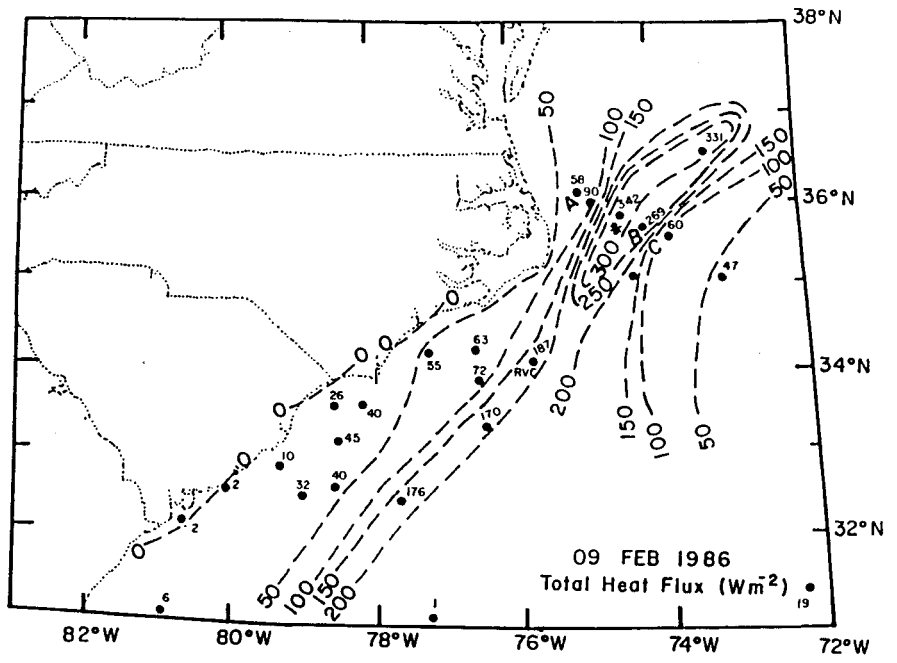
38°N
36°N
34°N
32°N
82°W
80°W
78°W
76°W
74°W
72°W
09 FEB 1986
Total Heat Flux (Wm⁻²)
RVC
A
B
C

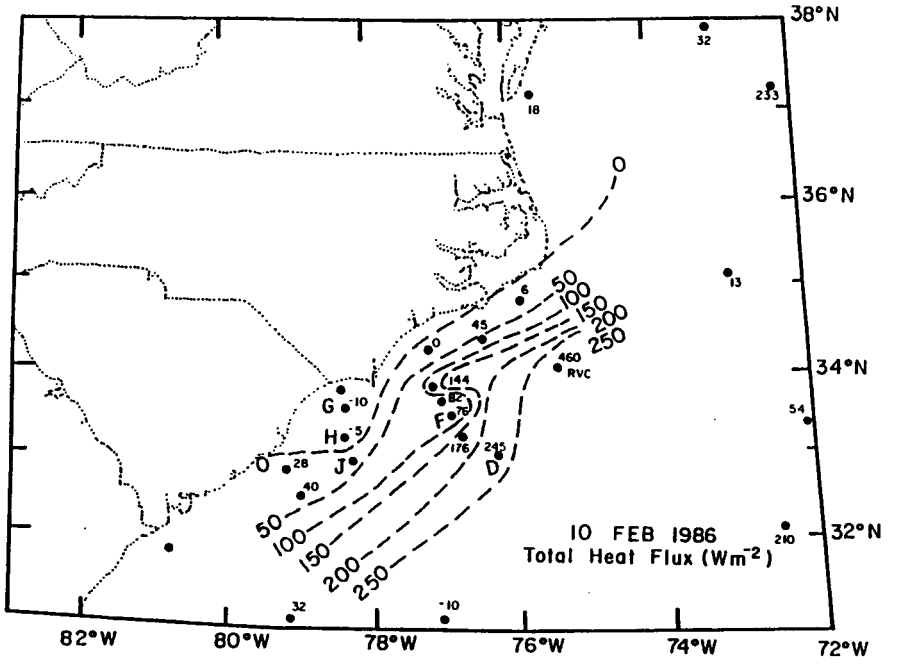
38°N
36°N
34°N
32°N
82°W
80°W
78°W
76°W
74°W
72°W
10 FEB 1986
Total Heat Flux (Wm⁻²)
RVC
D
F
G
H
J

Fig. 5(a, b).

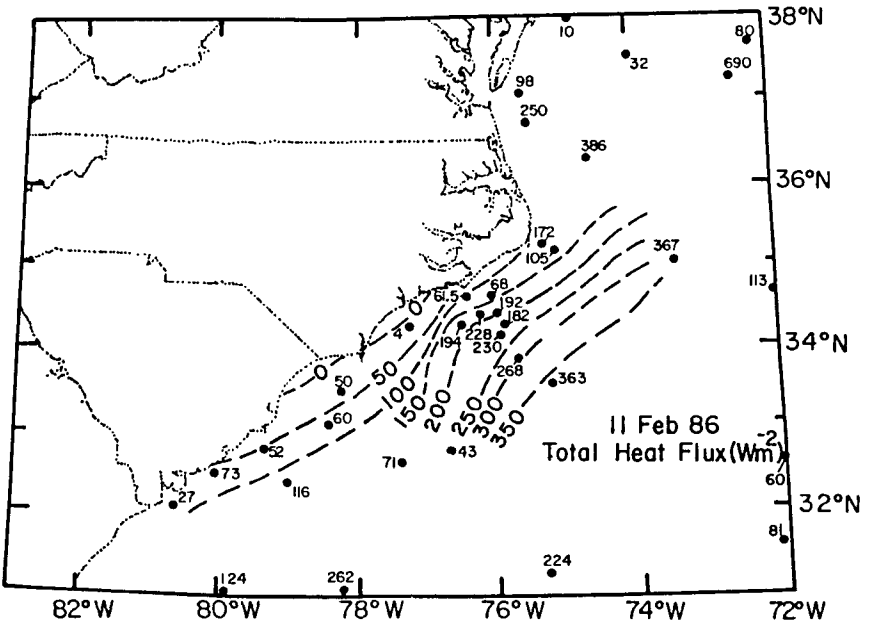

Fig. 5(c).

Fig. 5. Spatial variation of total surface turbulent heat fluxes (a) 9 February, (b) 10 February and (c) 11 February. Data obtained from buoy, ships and King Air and Electra aircraft data over the observation region.

4.2. Profiles of the turbulent fluxes of heat

Sensible heat flux profiles on 9, 10 and 11 February normalized by the near-surface value are shown in Figure 6. All values pertain to convective conditions. However, the degree of convection is different (see Table I for comparison) for each stack due to differences in the SST and its relative location to the storm. The solid line in the figure indicates the AMTEX data.

The normalized sensible heat fluxes ($\overline{w'\theta'}$) on 9 February over cold and warm waters (stacks A and B respectively) and on 10 February over warm waters (stack D) decreased almost linearly with height and became negative at approximately 0.85–$0.9h$. This result is in general agreement with observations over the Arabian Sea (Holt and Raman, 1986a) and during a cold air outbreak on January 28, 1986 (Wayland and Raman, 1989). However, the sensible heat flux profiles at stack J (represented by triangles) located just east of the divergence zone do not follow the simple linear relationship given above. This could be due to the appreciable horizontal inhomogeneity in the SST field with a significant variation in SSTs (18 °C to 22 °C). However, on 11 February a linear decrease in the normalized values was once again observed.

The normalized kinematic water vapor fluxes on all three days are shown in

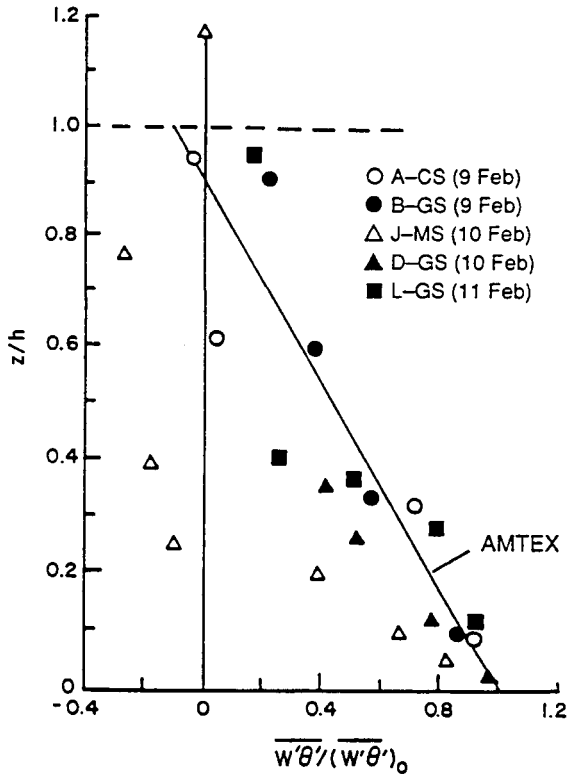

Fig. 6. Vertical profile of turbulent sensible heat flux normalized by the corresponding surface value. Locations A, B, J, D and L are as shown in Figure 1.

Figure 7. Normalized flux values on 9 February (represented by circles) show a linear decrease with height, becoming zero near the top of the boundary-layer. However, the profiles of $\overline{w'q'}$ on 10 February (triangles) do not follow this relationship but show an increase with height over the Gulf Stream which could be due to strong advection associated with the development of the offshore meso-low. On 11 February, a linear decrease in normalized values was observed over the Gulf Stream.

Thus, normalized sensible and latent heat fluxes appear to have reasonable similarity relations when conditions are quasi-stationary as on 9 February and where approximately homogeneous conditions exist as over the Gulf Stream on 11 February for sensible heat flux. When these conditions are violated, as on 10 February near the divergent regime or on 11 February over the Gulf Stream for water vapor flux, similarity relations break down.

4.3. Profiles of the Turbulent Fluxes of Momentum

Vertical variations of the wind stress, τ (N m^{-2}) in the vicinity of the Gulf Stream during various synoptic conditions are shown in Figure 8. The plotted values were

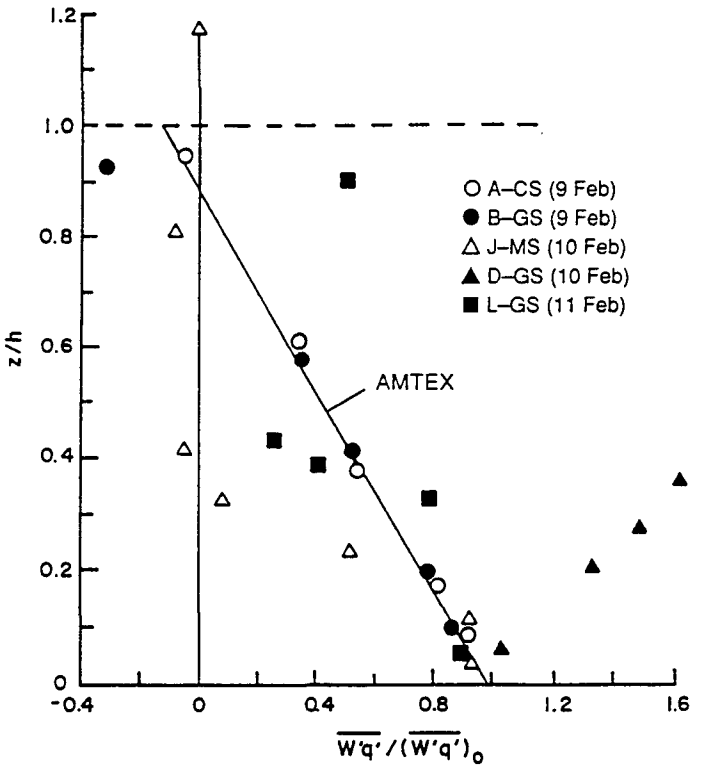

Fig. 7. Vertical profile of turbulent latent heat flux normalized by the corresponding surface value. Locations A, B, J, D and L are as shown in Figure 1.

calculated using along-wind ($\overline{u'w'}$) and crosswind ($\overline{v'w'}$) components of momentum flux. (The wind stress variation on 10 February is not shown due to lack of data above 250 m.) The MBL was convective at all three locations (A, B and L) although the degree of convection was different for each stack (Table I).

On 9 February over coastal waters, the wind stress near the surface was 0.12 N m^{-2}. It decreased to near zero at an altitude of 100 m. This profile over the cold water did not show any low-level acceleration. The surface wind stress over the Gulf Stream (B), on the other hand, was 0.21 N m^{-2}, which is approximately twice that observed over cooler waters. The wind stress at 100 m decreased to approximately half of the surface wind stress and then increased to a maximum of 0.23 N m^{-2} at a height of 210 m. This feature indicates the existence of low-level acceleration associated with a low-level jet caused by convergence near the western edge of the Gulf Stream. This is consistent with the mean profiles (not shown) which also show a low-level jet at this height. A low-level jet was also observed on 11 February, with maximum winds at 300 m height.

The surface wind stress on 11 February increased by a factor of three to about 0.65 N m^{-2}, as compared to 0.21 N m^{-2} on 9 February. These values are consistent

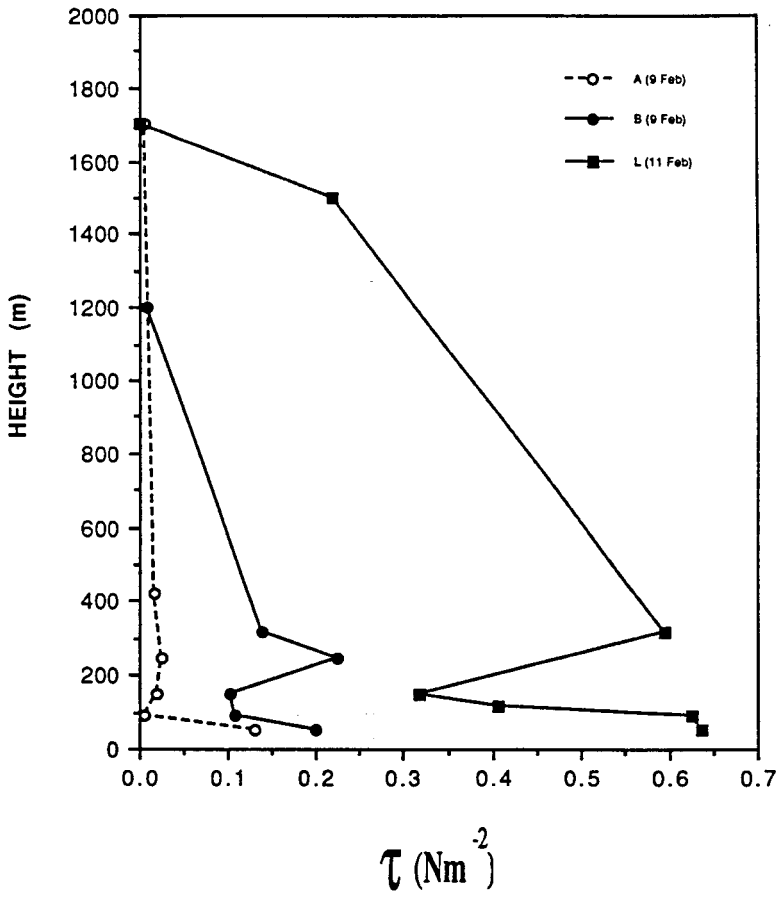

Fig. 8. Comparison of vertical profiles of wind stress over the colder coastal waters on 9 February with those over the warmer Gulf Stream waters on 9 and 11 February. Locations A, B and L are as shown in Figure 1.

with those obtained by Sethu Raman *et al.* (1986) during a five-day research cruise over the coastal Atlantic ocean off North Carolina ($0.15\,N\,m^{-2}$ before a cold frontal passage and $0.6\,N\,m^{-2}$ following the frontal passage). During a cold air outbreak of GALE (IOP#2), Wayland and Raman (1989) reported a surface wind stress of $0.3\,N\,m^{-2}$ over coastal waters and $0.7\,N\,m^{-2}$ over the Gulf Stream.

4.4. Power density spectra

Scales of turbulent motion in the vicinity of the Gulf Stream were examined utilizing power spectra during pre-storm and offshore cyclogenesis conditions. Spectra representative of the convective MBL over the colder coastal waters on 9 February are shown in Figure 9. Aircraft turbulence observations were made at

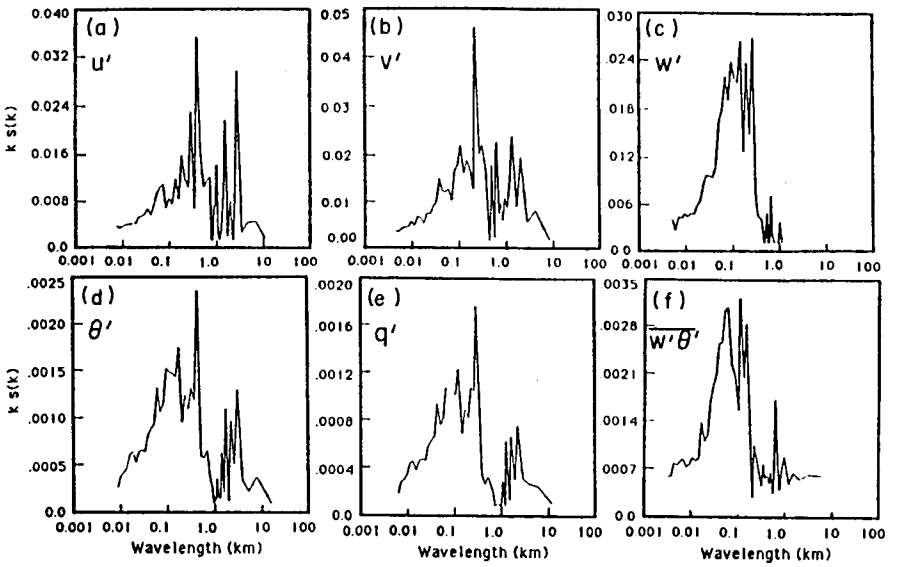

Fig. 9. Power density spectra and cospectra on 9 February over cold water (location A) at 40 m altitude for (a) u' ($m^2 s^{-2}$), (b) v' ($m^2 s^{-2}$), (c) w' ($m^2 s^{-2}$), (d) θ' (K^2), (e) q' ($g m^{-3}$)^2 and (f) $w'\theta'$ ($m s^{-1} K$).

an altitude of 40 m. Two significant peaks at 0.5 km and at about 3.5 km are evident in the spectra of the horizontal velocity components u' and v' (Figures 9a and 9b). The peak at 0.5 km is much stronger. The vertical velocity spectra, on the other hand, indicate dominant wavelengths of the order of 0.1 km. Spectra of temperature and moisture fluctuations (Figures 9d and 9e) are similar to the spectra of the horizontal wind but with smaller wavelengths (0.5–0.6 km). The cospectra between vertical velocity and temperature fluctuations indicate the dominant positive flux region to be between 0.01 and 0.5 km wavelengths with the peak near 0.1 km.

Spectra estimated from the turbulence observations at stack B over the Gulf Stream at 40 m altitude (Figure 10) are somewhat different from the spectra over the coastal waters. Spectra of the horizontal and vertical velocity fluctuations show a single, dominant peak with a wavelength between 0.7 and 0.9 km, approximately the height of the MBL (800 m). However, the vertical velocity spectra are much broader than those observed over cold waters. The peak wavelength of the temperature spectrum has shifted to 0.1 km with significant contributions up to 1 km wavelength. The moisture spectrum also shows a similar much broader spectrum with the dominant peak at 0.9 km wavelength. The overall effect of the broader spectra in w', H', q' is to produce a broader cospectrum. The dominant positive flux for $\overline{w'\theta'}$ is in the region of 0.1–1.2 km wavelength.

Dominant wavelengths corresponding to maximum energies from the spectra at

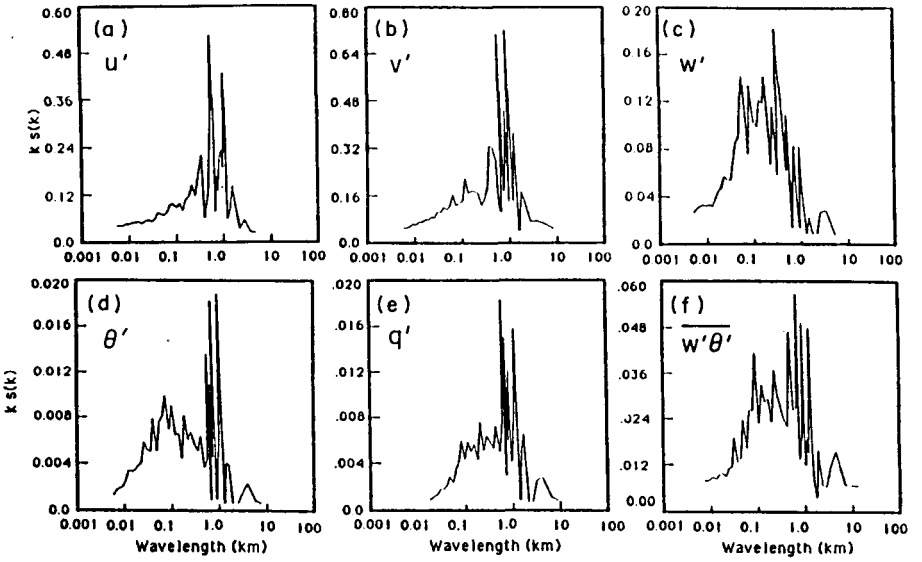

Fig. 10. Power density spectra and cospectra on 9 February over the Gulf Stream (location B) at 40 m altitude for (a) u' ($m^2 s^{-2}$), (b) v' ($m^2 s^{-2}$), (c) w' ($m^2 s^{-2}$), (d) θ' (K^2), (e) $(g m^{-3})^2$ and (f) $w'\theta'$ ($m s^{-1} K$).

the two locations (A and B) for different heights are given in Table II. Stack A was located over coastal waters and stack B was located over the Gulf Stream (see Figure 1 for location). These maximum energies were obtained by averaging energies at dominant wavelengths and the corresponding wavelengths by averaging the associated wavelengths. All the components have increased spectral energy over warmer waters with SST = 24 °C ($0.18 m^2 s^{-2}$), as compared to those over colder waters with a SST = 12 °C ($0.023 m^2 s^{-2}$) indicating the presence of more energetic eddies over warmer waters. Also, the dominant eddies are larger over the warmer Gulf Stream waters (0.4 km) as compared to coastal waters (0.2 km). This increase in wavelength by a factor of two is in response to the increase in boundary-layer height by about 50% over the Gulf Stream. Vertical velocity (w') spectra have an organized vertical structure, where the wavelengths corresponding to maximum energies are almost constant with height ($\lambda = 0.8$ km). However, over coastal waters the dominant wavelengths associated with the u' and v' spectra vary with height. These components are generally not as responsive to surface forcing and are affected more by advective processes.

At an altitude of 50 m over the coastal waters (coastal confluence, G), the spectra given in Figures 11a, 11b and 11c indicate dominant, well-defined peak wavelengths around 0.04 km and between 1 and 3 km for the u, v, and w components, respectively. Spectra of temperature fluctuations θ' (Figure 11d) and humidity fluctuations q' (Figure 11e) show dominant peaks at larger eddies, with less

TABLE II

Wavelengths (λ) corresponding to maximal spectral energy (E) on 9 February

Location	Height (m)	SST (°C)	U (m/s)	u'		v'		w'	
				λ km	E m^2/s^2	λ km	E m^2/s^2	λ km	E m^2/s^2
Cold Coastal Waters (air–sea temp. diff. = 2° C)									
A	40	10.23	5.8	0.60	0.020	0.60	0.020	0.2	0.023
A	100	10.46	6.6	1.00	0.030	1.00	0.060	0.8	0.100
A	150	10.45	6.63	0.70	0.035	0.70	0.025	0.8	0.021
A	280	10.50	5.4	0.60	0.035	1.00	0.035	0.8	0.025
Gulf Stream (air–sea temp. diff. = 9 °C)									
B	40	23.00	7.8	1.00	0.220	1.00	0.300	0.4	0.180
B	100	24.00	7.0	0.60	0.210	1.00	0.180	0.8	0.150
B	150	23.00	8.6	0.60	0.220	1.00	0.150	0.8	0.028
B	300	23.10	8.0	0.60	0.180	1.00	0.200	0.8	0.140

contributions from smaller wavelengths, indicating large-scale waves. The relatively small negative heat flux (-0.00075 K m s^{-1}) for the $\overline{w'\theta'}$ cospectrum is a result of an approximate balance between the positive flux from wavelengths near 0.5 km and negative flux of longer wavelengths between 0.6 and 2 km. The spectra over the near-shore shelf waters (just west of the divergence zone, H) also showed structure similar to that of the coastal waters. All the spectra were similar over the Gulf Stream on both days, perhaps because of large heat fluxes associated with strong convection.

Dominant wavelengths obtained from the spectra at G (coastal confluence over cold waters), H (near shore shelf waters), J (east of the diffluence zone) and the Gulf Stream (stack D) during the meso-low conditions (10 February) are given in Table III. A comparison of the w' spectral density values at all locations at altitudes of 90 and 150 m indicates maximum energy in the lower layers. At 150 m altitude (Table III), the dominant energies of vertical turbulence are negligible over the diffluence zone (H). The dominant energies increase towards both the confluence zones (G and J) situated on either side of the diffluence zone (H–J). A comparison of the profiles over the Gulf Stream and the cold shelf region indicates that the 0.9 km wavelength is not dominant over the cold shelf region. The spectra of w' has a maximum peak at 0.2–0.3 km over the midshelf as compared to a value of 0.6 km over the Gulf Stream. This is because of an increase in boundary-layer height by a factor of two over the Gulf Stream. The wind structure for each of the legs at different altitudes over the Gulf Stream is dominated by the eddies with 1–2 km wavelengths.

On 11 February, the spectra of u', v', q' and θ' show single peak maxima at wavelengths between 0.4 and 0.6 km (Table III). Vertical velocity spectra are much broader (not shown) with a single peak at 0.1 km. The spectral energy is larger over the Gulf Stream compared to the colder waters once again, indicating

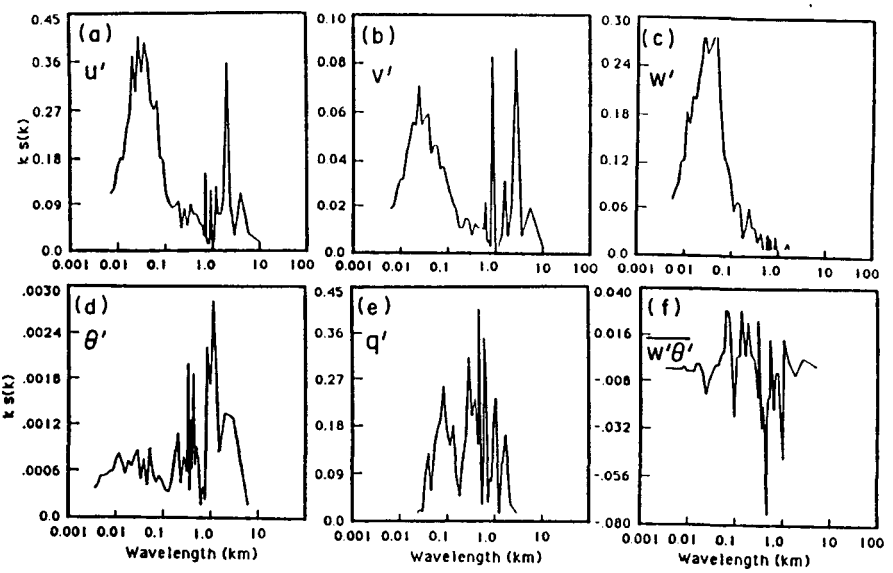

Fig. 11. Power density spectra and cospectra on 10 February over coastal waters (location G) at 50 m altitude for (a) u' ($m^2 s^{-2}$), (b) v' ($m^2 s^{-2}$), (c) w' ($m^2 s^{-2}$), (d) θ' (K^2), (e) q' ($g m^{-3}$)^2 and (f) $w'\theta'$ ($m s^{-1} K$).

that eddies are more energetic over warmer water. Also, an increase in spectral energy occurred as the storm developed over the Gulf Stream, indicating that the eddies become more energetic as the cyclone intensifies. The power density spectra also reveal that the size and energy of the dominant eddies increase towards the Gulf Stream. The dominant eddy over the divergence zone has negligible energy. Energies of the dominant eddies over the Gulf Stream increased from 9–10 February as the meso-low developed, and further increased on 11 February as the cyclone intensified.

4.5. Turbulent structure using conditional sampling

The bivariate conditional sampling technique proposed by Holland (1973) is used here. Holland assumed that the vertical flux of a passive scalar ζ can be decomposed into four components using a bivariate conditional sampling techniques. Thus for example:

$$\overline{w'\theta'} = \underset{\text{PP}}{\overline{w'_+\theta'_+}} + \underset{\text{NP}}{\overline{w'_+\theta'_-}} + \underset{\text{PN}}{\overline{w'_-\theta'_-}} + \underset{\text{NN}}{\overline{w'_-\theta'_+}}, \tag{3}$$

where, PP designates a positive flux P ($\overline{w'\theta'} > 0$) associated with a positive vertical velocity (P), PN designates a positive flux P ($\overline{w'\theta'} < 0$) associated with a negative vertical velocity (N), NP designates a negative flux N ($\overline{w'\theta'} < 0$) associated with a positive vertical velocity (P) and NN designates a negative flux N ($\overline{w'\theta'} < 0$)

TABLE III

Wavelengths (λ km) corresponding to maximum spectral energy, E (m/s) for 10–11 February, 1986 for u, v and w. Stack D is over the Gulf Stream, and Stacks G, H and J are over the confluence/difluence zones west of the Gulf Stream taken by the Electra on 10 February. Stacks L and K are over the Gulf Stream and Cold waters on 11 February respectively

Height (m)	Region	SST (C)	U m/s	u'				v'				w'			
				Peak 1		Peak 2		Peak 1		Peak 2		Peak 1		Peak 2	
				λ (km)	E	λ (km)	E	λ (km)	E	λ (km)	E	λ (km)	E	λ (km)	E
10 February (Gulf Stream, Stack D)															
40	D	24.69	10.1	1.00	0.10	–	–	1.00	0.09	–	–	0.25	0.09	–	–
90	D	24.43	9.8	1.00	0.10	–	–	1.00	0.10	–	–	0.40	0.12	–	–
150	D	24.00	9.9	1.00	0.05	–	–	0.090	0.06	–	–	0.50	0.11	–	–
250	D	23.50	9.0	2.00	0.10	–	–	2.00	0.12	–	–	0.50	0.11	–	–
10 February (G, H, J)															
90	G	10.00	7.5	0.80	0.34	2.00	0.20	0.18	0.18	4.00	0.13	0.80	0.40	2.00	0.05
90	H	14.00	5.5	0.03	0.22	2.00	0.06	0.15	0.03	2.00	0.04	0.04	0.18	–	–
90	J	20.00	2.6	0.50	0.04	–	–	0.40	0.04	2.00	0.2	0.10	0.06	–	–
150	G	10.00	6.7	0.70	0.010	–	–	1.00	0.04	5.00	0.06	1.00	0.03	–	–
150	H	14.00	3.6	0.15	0.002	1.50	0.02	0.20	0.02	2.00	0.03	0.20	0.01	1.5	0.01
150	J	20.00	4.6	0.50	0.006	–	–	0.50	0.04	–	–	0.13	0.07	–	–
11 February															
90	L	24.30	21.0	0.70	0.70	–	–	1.00	0.32	–	–	0.50	0.25	–	–
90	K	19.00	15.0	1.00	0.50	–	–	1.00	0.12	–	–	0.40	0.18	–	–

TABLE IV

Mean partitioned buoyancy fluxes (10^3 K cm/s) for 9 February for each aircraft leg. The percentage area occupied by each partition is given in parentheses. PP indicates positive flux associated with a positive vertical velocity, PN indicates a positive flux associated with a negative vertical velocity, NP indicates a negative flux associated with a positive vertical velocity and NN indicates a negative flux associated with a negative vertical velocity respectively

9 February: King Air stack	Height	SST	*U*	PP	PN	NP	NN	Total	Direct
		(°C)	(m/s)						(%)
(Cold Waters)									
A	40	10.2	5.8	12.82(34)	7.65(41)	−0.31(20)	−2.42(15)	15.3	65
A	90	10.4	6.6	9.55(27)	3.89(35)	−1.18(21)	−0.47(17)	11.8	62
A	150	10.4	6.6	3.0(23)	2.03(33)	−0.87(21)	−1.16(23)	2.9	56
A	280	10.5	5.4	2.19(26)	1.17(27)	−0.63(21)	−0.12(26)	1.5	53
A	400	10.5	7.0	2.55(28)	2.95(22)	−3.50(22)	−3.90(28)	−1.0	50
(Gulf Stream)									
B	40	23.1	7.81	85.41(28)	36.8(42)	−9.36(19)	−5.85(11)	117	70
B	90	24.0	6.97	46.4(30)	21.8(36)	−4.01(15)	−6.87(19)	57	66
B	150	23.1	8.63	70.4(26)	1.3(42)	−7.83(19)	−6.96(13)	87	68
B	300	23.3	8.00	17.7(41)	3.4(30)	−11.2(26)	−11.2(23)	8.6	51
B	450	22.0	7.00	10.11(27)	6.40(17)	−15.1(24)	−12.4(32)	−10	44

associated with a negative vertical velocity (N). Thus, thermally direct motions are given by PP (rising, positive buoyant air) and PN (sinking, negatively buoyant air). Thermally indirect motions are designated as NP and NN. Small-scale mixing (entrainment-detrainment) is identified as air moving laterally between cells. Air entrained into an upward moving cell or detrained from a downward moving cell is represented by NN, while air detrained from an upward moving cell or entrained from a downward moving cell is given by NP. In addition, entrainment occurring at the top of a cell and overshooting of parcels may contribute to the indirect flux or negative flux.

Statistics on the mean partitioned fluxes on 9 February estimated at stacks A (cold coastal waters) and B (Gulf Stream) are shown in Table IV for various levels in the boundary layer. The MBL consisted of discrete cell-like structures with a substantial contribution to the buoyancy flux from smaller less coherent elements. On 9 February, at 40 m altitude over the Gulf Stream, direct fluxes accounted for an average of 70% of the total time. For the same day, contributions by the direct mode were about 65% over the mid-shelf region at 40 m altitude. Contribution by the direct fluxes decreased with increasing height with direct and indirect fluxes almost equal (50%) at the top of the boundary layer. Similar results of 72 and 28% over the warmer Gulf Stream waters as direct and indirect modes respectively on 10 February have been observed (Table V) at an altitude of 40 m. The ratio of updraft area to downdraft area over the warm midshelf front and the warmer Gulf Stream are 0.85 and 0.61, which indicates that the intense, narrower warm updrafts dominate the total flux, but the broader, less intense, cool downdrafts

TABLE V

Mean partitioned buoyancy fluxes (10^3 K m/s) for 10–11 February for each aircraft leg. The percentage area occupied by each partition is given in parentheses. PP indicates positive flux associated with a positive vertical velocity, PN indicates a positive flux associated with a negative vertical velocity, NP indicates a negative flux associated with a positive vertical velocity and NN indicates a negative flux associated with a negative vertical velocity respectively

	Height	SST (°C)	U (m/s)	PP	PN	NP	NN	Total	Direct (%)
10 February: King Air									
(Cold Waters)									
D	40	24.7	10.1	32.2(28)	16.6(44)	−3.2(17)	−2.9(11)	44	72
D	90	24.4	9.8	31.4(28)	12.8(35)	−2.5(20)	−2.1(17)	40	63
D	150	24.0	9.9	23.8(23)	10.0(36)	−5.0(20)	−5.0(21)	24	59
D	250	23.5	9.0	13.6(28)	5.7(36)	−1.3(30)	−3.3(23)	15	64
Electra									
(Cold Waters)									
G	50	10.0	7.5	13.0(21)	13.4(30)	−12.8(26)	−11.7(23)	2	51
H	50	14.0	5.5	11.8(21)	14.9(27)	−17.2(31)	−12.0(21)	−2	48
Mid Shelf Waters									
J	50	20.0	2.6	9.2(27)	4.5(38)	−1.7(18)	−.0(17)	10	65
11 February (King Air)									
(Gulf Stream)									
L	30	24.4	21	47.5(28)	29.6(44)	−9.3(19)	−9.8(19)	58	72
(Mid Shelf Waters)									
K	30	18.0	15	28.2(20)	17.2(44)	−4.2(19)	−3.3(17)	38	64

occupy a larger portion of the transect over the Gulf Stream. The decrease in direct fluxes with height remained constant over the Gulf Stream on both days (9 and 10 February), perhaps because of strong convection.

The direct fluxes at stack G with a SST of 11 °C on 10 February over the coastal convergence zone (Table V) are slightly larger than at stack H located close to the divergence region but with a warmer SST of 14 °C. Larger direct fluxes are obviously caused by the mesoscale convergence. Also, the static stability at location H was greater than that at G. The total negative heat flux (as seen in the cospectrum of Figure 11f), is not entirely due to entrainment (NN). A significant portion of the negative flux is due to rising, cooler air (NP). In fact, NP (−17.2, 31%) occupies more than NN (−12.0, 21%). This suggests an indirect circulation. This region shows the lowest percentage of time occupied in the direct mode (48%) as compared to any other region on all three days.

Grossman (1984) estimated the partitioned fluxes over the tropical warmer waters as 64 and 36% in direct and indirect modes, respectively. Rogers (1989) during FASINEX (Frontal Air Sea Interaction Experiment; which is located roughly southwest of Bermuda 29 N, 70 W), estimated 62 and 38% over the warmer waters and 54 and 46% over colder waters in direct and indirect modes, respectively. Holt and Raman (1992) estimated 68 and 32% over the Gulf Stream and 56 and 44% over colder waters during an offshore coastal front event in direct

and indirect modes, respectively. For the present case, 70–72 and 28–30% are in direct and indirect modes, respectively, on all three days over the warmer waters (Tables IV and V). Mixing or indirect fluxes were a significant portion of the total flux. However, in the Atlantic trade winds near Barbados, the indirect fluxes were observed to be almost equally divided between entrainment and detrainment (Grossman, 1984).

4.6. Turbulence structure in the stable region

Internal gravity waves are known to co-exist with turbulence close to the surface during stable atmospheric conditions (Caughey and Readings, 1975) over land. These waves have also been observed in the marine surface layer during daytime conditions with a stably stratified atmospheric surface layer (SethuRaman, 1977). These waves tend to break because of shear instability but may reform again if conditions are conducive. Theoretical studies (Gossard and Hooke, 1975) and field observations (Ludlam, 1967; Woods, 1969) have shown that internal waves in the atmosphere and oceans become unstable as the local Richardson number becomes less than about 0.25. Layers with Richardson numbers greater than 0.25 tend to have stable propagating waves.

As mentioned in Section 3, two convergence zones were present on 10 February, one over the coastal waters and the other near the western edge of the Gulf Stream with a divergence region between the two (see Figure 4). Electra aircraft data indicated a stable region along the Carolina coast (Figure 5b). The spatial variation of instantaneous wind speed, vertical velocity and air–sea temperature difference ($\Delta T = T_{air} - T_{water}$) for the transect G–J taken by the Electra aircraft are shown in Figure 12. From this transect (Figure 12a), Region IV is identified as the divergence zone (weak winds of 1–2 m s^{-1}), Region I and Region V are the two convergence zones over the coastal waters and the Gulf Stream, respectively. A Richardson number of 2.1 was estimated in this stable region.

Next we consider the transect at 50 m altitude flown by the Electra on 10 February from coastal waters (G) towards the warmer waters (J) which was approximately 106 km long. Patchy turbulence was observed over the cold waters as shown in Figure 12b. Instantaneous vertical velocities reached values up to 2 m s^{-1}, which is typical of strong convective flows. The boundary layer was stable over this region (west of the divergence zone, not shown) because of the advection of warmer air over relatively colder water. The time series of RH (not shown) for transects at all levels indicated clouds over this region. The pockets of turbulence over colder waters (Figure 12b) indicate the breaking of internal waves.

Typical energy spectra in this region are shown in Figure 11. The peak of the spectrum occurred at a wavelength of 0.03 km. Harmonics of this dominant wave can be seen at higher wavelengths in the $\overline{w'\theta'}$ spectrum (Figure 11f). The increase in energy at higher wavelengths might be due to the process of wave breaking that enhances turbulence.

Variances and covariances of velocity fluctuations and potential temperature

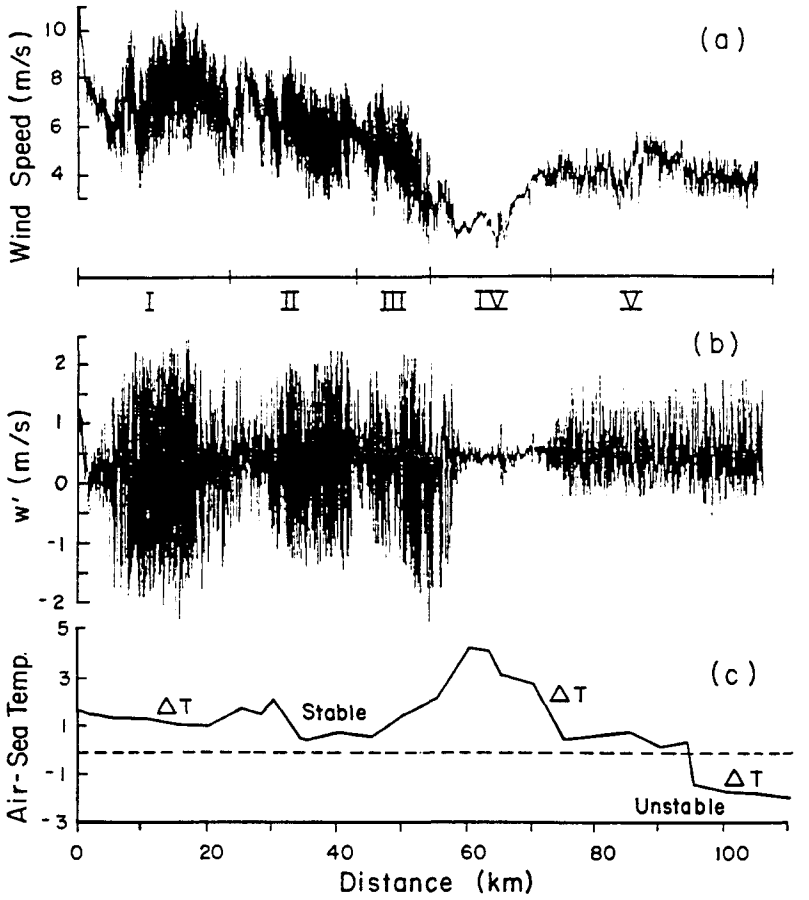

Fig. 12. Spatial variation of instantaneous (a) wind ($m\,s^{-1}$), (b) vertical velocity, w' ($m\,s^{-1}$) and (c) air–sea temperature difference observed by the Electra aircraft at 50 m altitude from G to J (Figure 1). Distances are from the aircraft speed of $110\,m\,s^{-1}$.

over cold waters (G) at three different altitudes (50, 90 and 150 m) are given in Table VI. Mean wind speeds did not vary much at three different altitudes (Figure 12a), but the turbulence varied significantly. Variance of u is greater than the variance of v, probably due to the propagation of waves in the longitudinal direction. Also, σ_w has higher values (of the order of $0.8–1.0\,m\,s^{-1}$) in the intermittent turbulence region, as expected. Turbulent fluxes $\overline{u'w'}$ and $\overline{v'w'}$ are positive, indicating an upward transfer of momentum. Upward momentum flux and increased turbulence during wave-breaking phenomena were also observed by SethuRaman (1980) in the MBL and in a frontal surface (Ley and Peltier, 1978). Not much is known about wave breaking, which may involve overturning,

TABLE VI

Turbulence statistics in the stable region

Variables	$z = 50$ m	$z = 90$ m	$z = 150$ m
σ_u (m s^{-1})	0.89	0.63	0.25
σ_v (m s^{-1})	1.09	0.77	0.32
σ_w (m s^{-1})	0.44	0.38	0.28
σ_T (K)	0.08	0.10	0.05
$\overline{u'w'}$ (m^2 s^{-2})	0.1	0.07	0.017
$\overline{v'w'}$ (m^2 s^{-2})	0.04	0.001	−0.002
$\overline{w'\theta'}$ (m s^{-1} K)	−0.01	−0.002	0.00
$\overline{w'e'}$ (m^3 s^{-3})	0.031	0.015	0.005

shear instability, convective instability, resonant interaction (Thorpe, 1975), and wave turbulence interaction (Chimonas, 1972).

4.7. Turbulent kinetic energy budget

Assuming horizontal homogeneity, the TKE budget in the MBL can be expressed as:

$$\frac{\partial \bar{e}}{\partial t} = -\overline{u'w'}\frac{\partial U}{\partial z} - \overline{v'w'}\frac{\partial V}{\partial z} + \frac{g}{\bar{\theta}_v}\overline{w'\theta_v'} - \frac{\partial}{\partial z}(\overline{w'e}) - \frac{1}{\bar{\rho}}\frac{\partial}{\partial z}(\overline{w'p'}) - \epsilon\,, \tag{4}$$

where turbulent kinetic energy $\bar{e} = 0.5(\overline{u'^2} + \overline{v'^2} + \overline{w'^2})$, and p' is the fluctuating pressure and is the energy dissipation rate. The first two terms on the right-hand side of Equation (4) are along-wind and crosswind shear production (S), the third term is buoyancy production (B), the fourth is turbulent transport (T), the fifth is pressure transport (P) and the sixth is viscous dissipation (D). The left-hand side of the equation is the local change of TKE. It includes horizontal and vertical advection and temporal changes. Hence, the TKE budget can be expressed as:

$$\text{Local Change of TKE} = \text{S} + \text{B} + \text{T} + \text{P} + \text{D} + \text{I}\,, \tag{5}$$

where I is the imbalance in the TKE due to errors in the estimation of all the terms. The term I here also includes any errors in the assumption of stationary and homogeneous conditions. Turbulent transport was obtained from finite differencing of the turbulence energy flux $\overline{w'e'}$ shown in Figure 13. The normalized data below $0.6h$ of the MBL are fit well by,

$$\overline{we}/w_*^3 = 0.82(z/h)(1 - 9z/h)^2 \tag{6}$$

at both stacks A and B on 9 February and stack D (Gulf Stream) on 10 February. Other observational studies have found a similar relationship but with different values for the constant 0.82. For GALE, during an offshore redevelopment of a

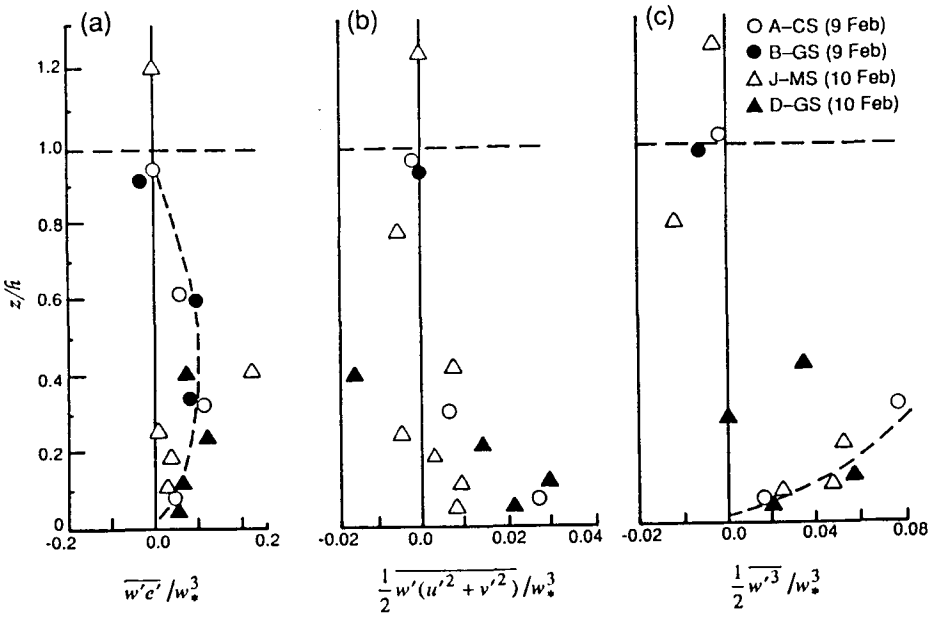

Fig. 13. Profiles of (a) vertical turbulent transport of energy, (b) vertical flux of horizontal variance and (c) vertical flux of vertical variance. Dotted lines are best-fit curves.

cyclone, this constant was found to be 0.5 (Holt and Raman, 1990). For other observational studies, this constant was found to be roughly the same for AMTEX (Lenschow *et al.*, 1980) and 1.2 for MASEX (Chou *et al.*, 1986), respectively. However, the values at stack J (represented as triangles in the Figure 13) over mid-shelf waters on 10 February follow the curve. Also they are near zero above $0.15h$, indicating that turbulent transport is insignificant in the vicinity of the divergence zone.

The relative contribution from the horizontal and vertical velocity variances to the vertical flux of the TKE are shown in Figures 13b and 13c. The horizontal flux variance dominates $\overline{w'(u'^2 + v'^2)}$ near the surface due to increased shear generation. If the stack J is excluded, the normalized vertical flux of vertical velocity variance $0.5\overline{w'^3}/w_*^3$ has a relationship of the form,

$$\overline{w'^3}/w_*^3 = 0.54(z/h)(1 - 0.8z/h)^2 \tag{7}$$

in the lowest third of the MBL. Other observational studies have found a similar relationship but with different values for the constant. For GALE during an offshore cyclogenesis, Holt and Raman (1991) found the constant to be 0.32. The AMTEX and MASEX studies found the constant to be 0.75 and 1.8, respectively. The ratio of the vertical fluxes of horizontal and vertical velocity variance $\overline{w'(u'^2 + v'^2)}/\overline{w'^3}$ (as can be inferred from the figure) is slightly greater than one

in the surface layer and less than one throughout the MBL. This indicates a larger contribution of vertical velocity variance to turbulent transport, $\overline{w'e'}/w_*^3$.

The buoyancy production term was estimated from the mean potential temperature and sensible heat flux between two adjacent flight levels using a simple finite difference method. Similarly, shear production was estimated from the shear stress and wind shear between two adjacent levels using the finite differencing scheme. Viscous dissipation (ϵ) was obtained from the inertial subrange of the vertical velocity spectra. For the present case, pressure transport was not measured but was obtained using a relation given by Zeman and Lumley (1976).

Horizontal homogeneity can be assumed to be valid for 9 February as the computed values of along-wind ($-u'(\partial\bar{e}/\partial x)$) advection of TKE ($10^{-5}\,m^2\,s^{-3}$) are three orders of magnitude less than the other components (10^{-2}–$10^{-3}\,m^2\,s^{-3}$) in the budget. Accurate estimation of the crosswind ($-v'(\partial\bar{e}/\partial y)$) advection of TKE is very difficult. In contrast, horizontal homogeneity was not valid for 10 February as the computed values of along-wind advection of TKE ($10^{-3}\,m^2\,s^{-3}$) are almost of the same magnitude as that of other components in the budget at locations J and D.

The normalized TKE budget over the Gulf Stream (B) on 9 February is shown in Figure 14. The profiles are normalized by w_*^3/h on the horizontal coordinate and by boundary-layer height for the vertical coordinate. The values of w_* and h are given in Table I. The TKE budget over the Gulf Stream is different from that compared to the TKE budget over colder waters (not shown). Shear production dominates throughout the MBL but the buoyancy production is also significant. Increased importance of shear in the MBL is due to strong convergence at the western boundary of the Gulf Stream which resulted in increased wind speeds at this location. A low-level jet at $0.2h$ is clearly seen in the shear production profile. Huang and Raman (1988) also found this low-level acceleration of the wind field in the vicinity of the Gulf Stream front using a two-dimensional second-order closure model. They attributed this feature to the baroclinic effects found in the MBL during cold air outbreaks. However, the present study is not a cold air outbreak situation. Vertical transport of TKE is negative below $0.4h$, indicating a net loss of energy from these lower layers, in good agreement with results from studies of a cold air outbreak (Wayland and Raman, 1989), a monsoon MBL (Holt and Raman, 1986a, b) and earlier studies of a convective MBL (Lenschow *et al.*, 1980 and Chou *et al.*, 1986). Dissipation once again decreases linearly with height becoming almost zero near $z = h$. The imbalance term is a source term in the MBL throughout the MBL. The comparison of the vertical variation of imbalance over the Gulf Stream shows similar shape to that observed during GALE and MASEX (Chou *et al.*, 1986). The crossover point for the imbalance curve was observed to be at $0.9h$ compared to $0.8z/h$ for cold air outbreaks during GALE (Wayland and Raman, 1989) and much lower levels during MASEX. The major difference of the imbalance curve during GALE compared to MASEX is the large imbalance at the surface. However, this agrees with the large shear

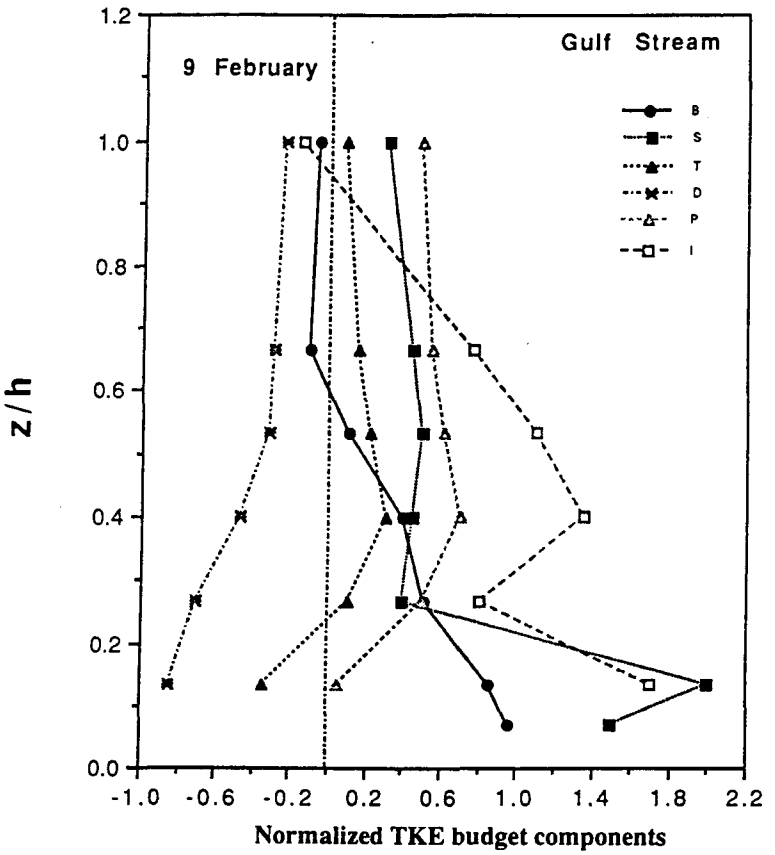

Fig. 14. TKE budget components normalized by w_*^3/h at Stack B over the Gulf Stream on 9 February. The components are buoyancy production (B), shear production (S), turbulent transport (T), pressure transport (P), dissipation (D) and imbalance (I).

production values measured at low levels during GALE as compared to the MASEX data. From this analysis on 9 February, one process that could reduce the low-level imbalance would be crosswind advection of TKE, which cannot be accurately estimated for this particular data set. Another reason for the large imbalance could be the approximate nature of the determination of pressure transport and the other measurement errors.

The normalized TKE budget on 10 February over the Gulf Stream (D) is shown in Figure 15. The TKE budget is plotted only up to $0.4h$ due to the lack of data above. Buoyancy production dominates at least up to $0.4h$. Shear production decreases from a maximum at the surface to zero at $0.3h$, and becomes negative above. Dissipation is the major sink term, once again decreasing monotonically with height. The turbulent transport term appears to be insignificant. However,

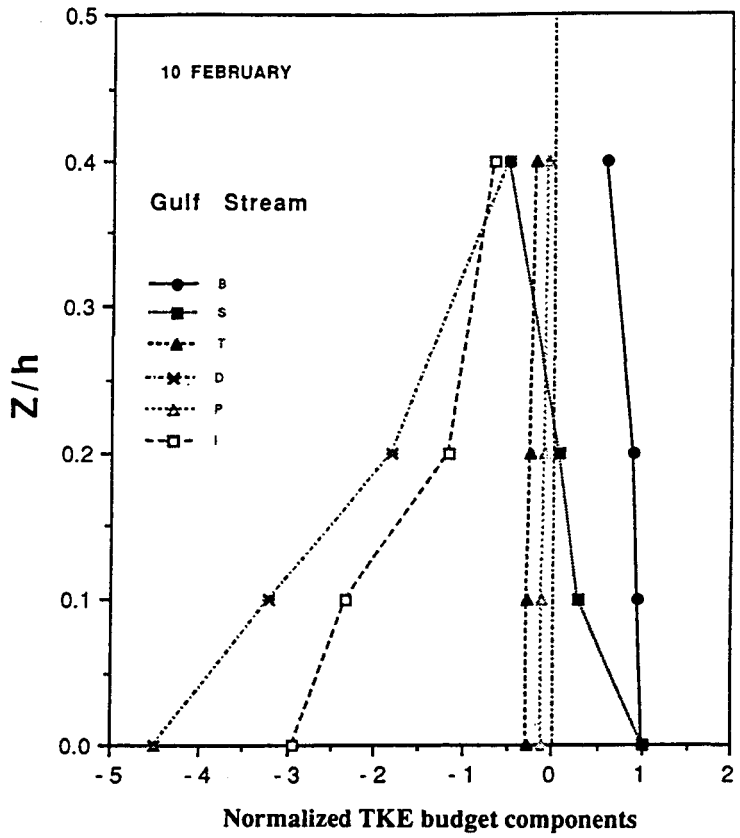

Fig. 15. TKE budget components normalized by w_*^3/h at Stack D over the Gulf Stream on 10 February. The components are buoyancy production (B), shear production (S), turbulent transport (T), pressure transport (P), dissipation (D) and imbalance (I).

the large imbalance can be attributed to the assumption of homogeneity, which may not be valid during a developing meso-low.

A comparison of TKE budgets on both days (9 and 10 February) over the Gulf Stream indicates that the buoyancy production is more important during a developing meso-low as opposed to clear conditions. Shear production is almost insignificant on 10 February. Dissipation increases from 9 February to 10 February over the Gulf Stream. The existence of an imbalance term is in agreement with other studies (AMTEX and MASEX) on 9 February (Figure 14). On 10 February, imbalance is a major sink term (Figure 15), perhaps because of the assumption of homogeneity and steady state conditions during disturbed weather conditions. Therefore, the TKE budget on 9 February is in good agreement with others under conditions closer to free convection (Lenschow *et al.*, 1980; Wills and Deardorff,

1974). Also, the budget is fairly well balanced on 9 February in the middle of the MBL.

5. Conclusions

Turbulent MBL structure and mesoscale circulation features were compared for three synoptic situations over the Gulf Stream and the cold coastal waters. Power density spectra indicate that the size and energy of the eddies were greater over the Gulf Stream due to an increase in convection. Results using conditional sampling techniques suggest that it is the intense narrower warm updrafts that dominate the total heat flux. The broader, less intense cool downdrafts seem to occupy a large portion of the Gulf Stream. The values of direct and indirect fluxes are larger as compared to observations over the tropical ocean by Grossman (1984) but close to observations over the Gulf Stream by Holt and Raman (1992). Observational data over a stable region near the coast on 10 February indicates the existence of internal gravity waves. Intermittent turbulence observed over this region suggests wave breaking phenomena.

A comparison of TKE budgets on two days (9 and 10 February) with different weather events over the Gulf Stream indicates that the buoyancy production is more important during a developing meso-low as opposed to quiescent conditions. Shear production during meso-low development (10 February) is small compared to the values on 9 February during pre-storm conditions.

Acknowledgements

Authors wish to thank Dr. Teddy Holt for several helpful suggestions. This study was supported by the Division of Atmospheric Sciences, National Science Foundation under grant ATM-92-12636 and by the Department of Energy under contract 091575-A-Q1 with Pacific Northwest Laboratories.

References

Brown, E. N., Friehe, C. A., and Lenschow, D. H.: 1983, 'The Use of Pressure Fluctuations on the Nose of an Aircraft for Measuring Air Motion', *J. Climate Appl. Meteorol.* **22**, 171–180.

Caughey, S. J. and Readings, C. J.: 1975, 'An Observation of Waves and Turbulence in the Earth's Boundary-Layer', *Boundary-Layer Meteorol.* **9**, 279–296.

Chimonas, G.: 1972, 'The Stability of a Coupled Wave-Turbulence System in a Parallel Shear Flow', *Boundary-Layer Meteorol.* **2**, 444–452.

Chou, S. H., Atlas, D., and Yeh, E.-N.: 1986, 'Turbulence in a Convective Marine Atmospheric Boundary-Layer', *J. Atmos. Sci.* **43**, 547–564.

Dirks, R. A., Kuettner, J. P., and Moore, J. A.: 1988, 'Genesis of Atlantic Lows Experiment (GALE): An Overview', *Bull. Amer. Meteorol. Soc.* **69**, 148–160.

Gossard, E. E. and Hooke, W. H.: 1975, *Waves in the Atmosphere*, Elsevier Scientific Publishing Company, New York, 456 pp.

Grossman, R. L.: 1984, 'Bivariate Conditional Sampling of Moisture Flux over a Tropical Ocean, *J. Atmos. Sci.* **41**, 3228–3253.

Herbster, C. G.: 1990, 'The Vertical Structure of the Marine Atmospheric Boundary-Layer Across a Sea Surface Temperature Front', M.S. Thesis, Department of Meteorology, Florida State University, 164 pp. [Available from Dept. of Meteorology, Florida State University, Tallahassee, FL 32306-3034.]

Holland, J. Z.: 1973, 'A Statistical Method for Analyzing Wave Shapes and Phase Relationships of Fluctuating Geophysical Variables', *J. Phys. Oceanogr.* **3**, 139–155.

Holt, T. and Raman, S.: 1986a, 'Variation of Turbulence in the Marine Boundary-Layer Over the Arabian Sea during Indian Southwest Monsoon (MONEX 79), *Boundary-Layer Meteorol.* **37**, 71–87.

Holt, T. and Raman, S.: 1986b, 'Observations of the Mean and Turbulence Structure of the Marine Boundary-Layer over the Bay of Bengal During MONEX 79', *Mon. Wea. Rev.* **114**, 2176–2190.

Holt, T. and Raman, S.: 1990, 'Marine Boundary-Layer Structure and Circulation in the Region of Offshore Redevelopment of a Cyclone During GALE, *Mon. Wea. Rev.* **118**, 392–410.

Holt, T. and Raman, S.: 1992, 'Three Dimensional Mean and Turbulence Structure of a Coastal Front Influenced by the Gulf Stream', *Mon. Wea. Rev.* **120**, 17–39.

Haung, C. Y. and Raman, S.: 1988, 'A Numerical Modeling Study of the Marine Boundary-Layer Over the Gulf Stream During Cold Air Advection', *Boundary-Layer Meteorol.* **45**, 251–290.

Haung, C. Y., and Raman, S.: 1989, 'An Application of the E–ϵ Closure Model to Simulations of Mesoscale Topographical Effects', *Boundary-Layer Meteorol.* **49**, 169–195.

Haung, C. Y. and Raman, S.: 1990, 'Numerical Simulations of Cold Air Advection Over the Appalachian Mountains and the Gulf Stream', *Mon. Wea. Rev.* **118**, 343–362.

Haung, C. Y. and Raman, S.: 1991a, 'Numerical Simulation of January 28 Cold Air Outbreak During GALE. Part I: The Model and Sensitivity Tests of Turbulence Closures', *Boundary-Layer Meteorol.* **55**, 381–407.

Haung, C. Y. and Raman, S.: 1991b, 'Numerical Simulation of January 28 Cold Air Outbreak During GALE. Part II: The Mesoscale Circulation and Marine Boundary-Layer', *Boundary-Layer Meteorol.* **56**, 51–81.

LeMone, M. A. and Pennell, W. T.: 1980, 'A Comparison of Turbulence Measurements from Aircraft', *J. Appl. Meteorol.* **19**, 1420–1437.

LeMone, M. A.: 1973, 'The Structure and Dynamics of Horizontal Roll Vortices in the in the Planetary Boundary-Layer', *J. Atmos. Sci.* **30**, 1077–1091.

Lenshow, D. H. and Spyers-Duran, P.: 1986, 'Measurement Techniques: Air Motion Sensing', NCAR Bulletin No. 23. [NCAR, Boulder, CO 80307.]

Lenschow, D. H., Wyngaard, J. C., and Pennell, W. T.: 1980, 'Mean-Field and Second-Moment Budgets in a Baroclinic, Convective Boundary-Layer', *J. Atmos. Sci.* **37**, 1313–1326

Ley, B. and Peltier, W. R.: 1978, 'Wave Generation and Frontal Collapse', *J. Atmos. Sci.* **35**, 3–17.

Lind, R. J. and Shaw, W. J.: 1990, 'The Time-Varying Calibration of an Airborne Lyman-α Hygrometer', *J. Atmos. Oceanic Technol.* **8**, 186–190.

Ludlam, F. H.: 1967, 'Characteristics of Billow Clouds and their Relation to Clear-Air Turbulence', *Q. J. R. Meteorol. Soc.* **93**, 419–435.

Mercer, T. J. and Kreitzberg, C. W.: 1986, 'GALE Field Program Summary', Dept. of Physics and Atmospheric Sciences, Drexel University, Philadelphia, PA 19104.

Raman, S. and Riordan, A. J.: 1988, 'The Genesis of Atlantic Lows Experiment: The Planetary Boundary-Layer Subprogram, *Bull. Amer. Meteorol. Soc.* **69**, 161–172.

Rogers, D. P.: 1989, 'The Marine Boundary Layer in the Vicinity of an Ocean Front', *J. Atmos. Sci.* **46**, 2044–2062.

Sethu Raman, S.: 1977, 'The Observed Generation and Breaking of Atmospheric Internal Gravity Waves Over the Ocean', *Boundary-Layer Meteorol.* **12**, 331–349.

Sethu Raman, S.: 1980, 'A Case of Persistent Breaking of Internal Gravity Waves in the Atmospheric Surface Layer Over the Ocean', *Boundary-Layer Meteorol.* **19**, 67–80.

Sethu Raman, S., Riordan, A. J., Holt, T., Stunder, M., and Hinman, J.: 1986, 'Observations of the Marine Boundary-Layer Thermal Structure Over the Gulf Stream During a Cold-Air Outbreak', *J. Appl. Clim. Meteorol.* **25**, 14–21.

Thorpe, S. A.: 1975, 'The Excitation, Dissipation, and Interaction of Internal Waves in the Deep Ocean', *J. Geophys. Res.* **80**, 328–338.

Wai, M. M.-K and Stage, S. A.: 1989, 'Dynamical Analysis of Marine Atmospheric Boundary-Layer Structure Near the Gulf Stream Oceanic Front', *Q. J. R. Meteorol. Soc.* **115**, 29–44.

Wayland, R. J. and Raman, S.: 1989, 'Mean and Turbulent Structure of a Baroclinic Marine Boundary-Layer During the 28 January 1986 Cold-Air Outbreak (GALE 86)', *Boundary-Layer Meteorol.* **48**, 227–254.

Wills, G. E. and Deardorff, J. W.: 1974, 'A Laboratory Model of the Unstable Planetary Boundary-Layer', *J. Atmos. Sci.* **31**, 1297–1307.

Woods, J. D.: 1969: 'Wave-Induced Shear Instability in the Summer Thermocline', *J. Fluid Mech.* **32**, 791–800.

Wyngaard, J. C., Cote, O. R., and Izumi, Y.: 1971, 'Local Free Convection, Similarity and the Budgets of Shrear Stress and Heat Flux', *J. Atmos. Sci.* **28**, 1171–1182.

Zeman, O. and Lumley, J. L.: 1976, 'Modeling Buoyancy Driven Mixed Layers', *J. Atmos. Sci.* **33**, 1974–1988.